nature energy

Supplementary information

https://doi.org/10.1038/s41560-024-01638-z

In situ formation of liquid crystal interphase in electrolytes with soft templating effects for aqueous dual-electrode-free batteries

In the format provided by the authors and unedited

Table of contents:

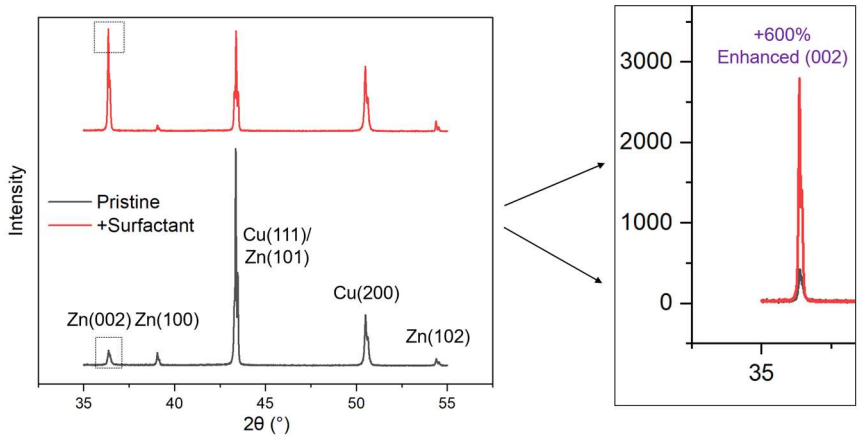

Supplementary Fig. 1.
XRD analysis of Zn metals on bare Cu foil formed in the DEFBs using the pristine electrolyte or surfactant electrolyte after 10 cycles (charging at 2.3 V up to 0.5 mAh/cm² and discharging at 5 mA/cm² down to 1 V).

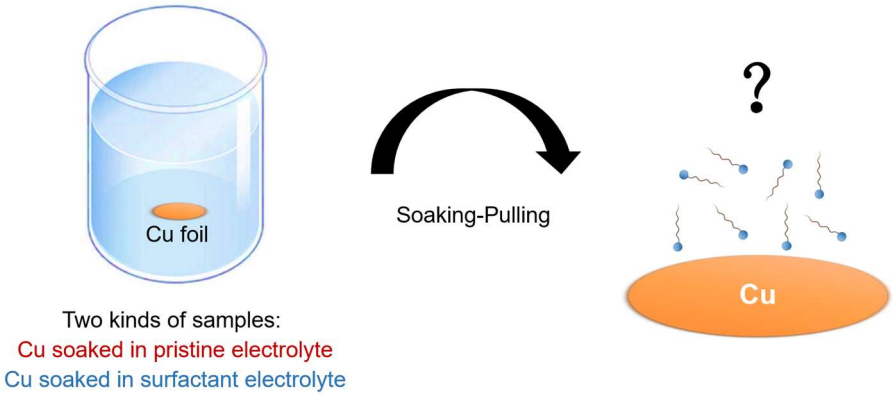

Supplementary Fig. 2.
Schematic illustrating the sample preparation (Cu foil soaked in the pristine electrolyte or surfactant electrolyte) for identifying the alignment of surfactant molecules before deposition.

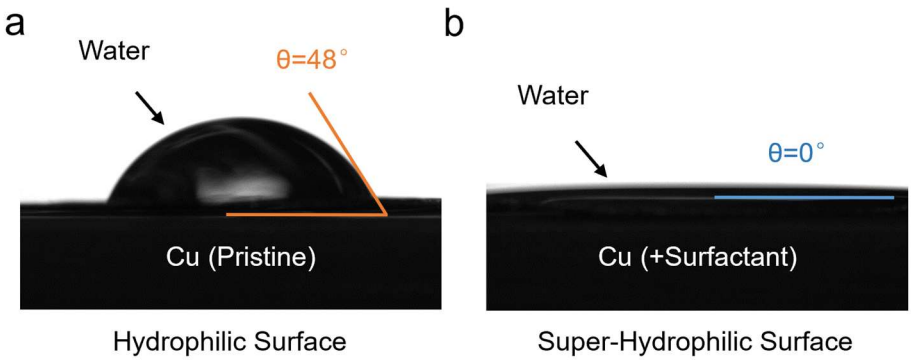

Supplementary Fig. 3.
Contact angle tests of water on bare Cu after immersion of the pristine electrolyte (a) or surfactant electrolyte (b).

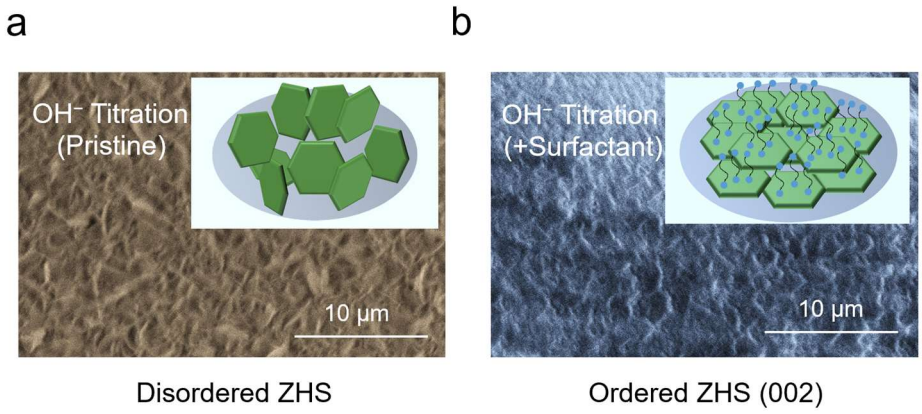

Supplementary Fig. 4.
Chemical titration experiments (by introducing an alkaline solution: $4Zn^{2+}$ (aq) + $6OH^-$ (aq) + SO_4^{2-} (aq) + $5H_2O$ (l) → $Zn_4(OH)_6(SO_4)\cdot 5H_2O$ (s) (ZHS) ↓) on bare Cu covered by the pristine electrolyte (a) or surfactant electrolyte (b). Insets: Schematics illustrating the disordered ZHS (a) and ordered ZHS guided by surfactant molecules (b).

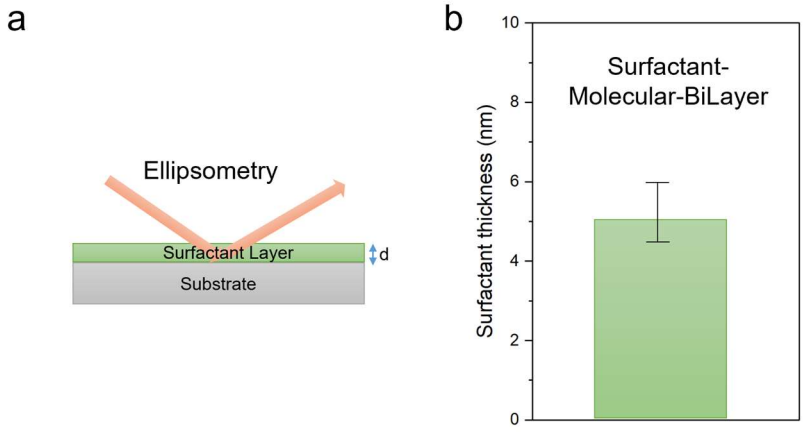

Supplementary Fig. 5.

Schematic illustrating the test principle of ellipsometry (a). Ellipsometry test of surfactant molecules on bare Cu (b). The measurements at various points on the coated Cu foil (dried state) are conducted to investigate the polarization change upon reflection from the coated Cu. It's worth noting that in this particular test, we exclusively utilized water and surfactant in the electrolyte to eliminate any potential salt interference. The error bar (standard deviation) of thickness data was obtained by five samples from different batches. The average used is the mean value. The data of this Figure are presented as the mean values ± standard error of the mean.

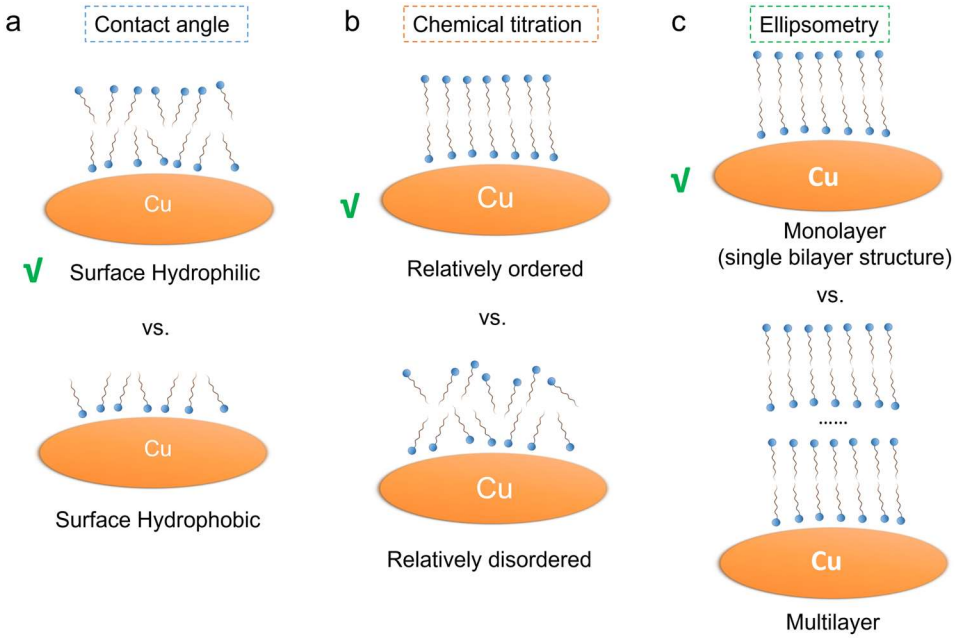

Supplementary Fig. 6.

Schematic illustrating the sample preparation (Cu foil soaked in different electrolytes) for identifying the alignment of surfactant molecules before deposition.

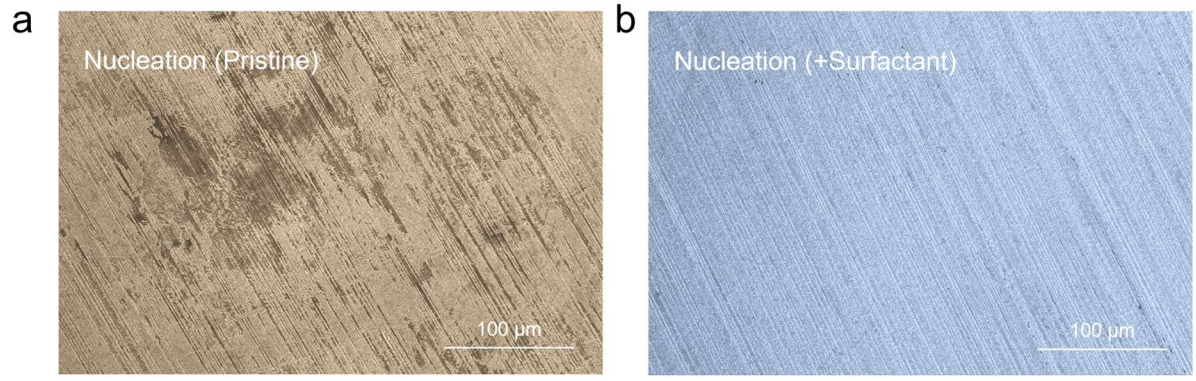

Supplementary Fig. 7.
SEM images of Zn formed in the DEFBs using the pristine electrolyte (a) or surfactant electrolyte (b). Deposited capacity is set as 50 μAh to investigate the nucleation process (constant voltage of 2.3 V). The pristine electrolyte leads to uneven nucleation, and sections of the copper foil were left exposed. In contrast, the surfactant electrolyte can promote uniform nucleation with fine Zn particles, effectively covering the entire Cu foil.

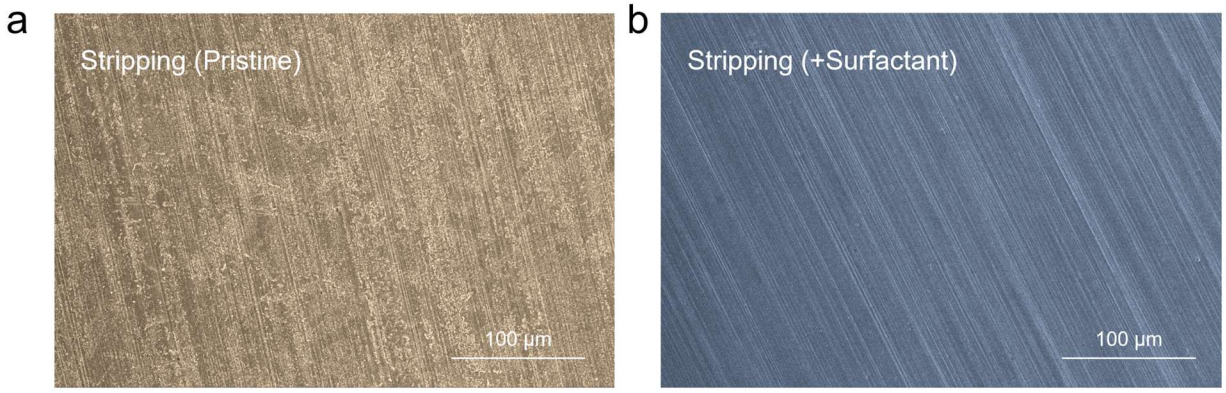

Supplementary Fig. 8.
SEM images of Zn stripping in the DEFBs using the pristine electrolyte (a) or surfactant electrolyte (b) after 10 cycles (charging at 2.3 V up to 0.5 mAh/cm² and discharging at 5 mA/cm² down to 1 V). In the pristine electrolyte, a substantial residue is observed on the Cu surface following Zn stripping, possibly indicative of inactive Zn. Conversely, the use of surfactant electrolyte results in a relatively clean Cu surface.

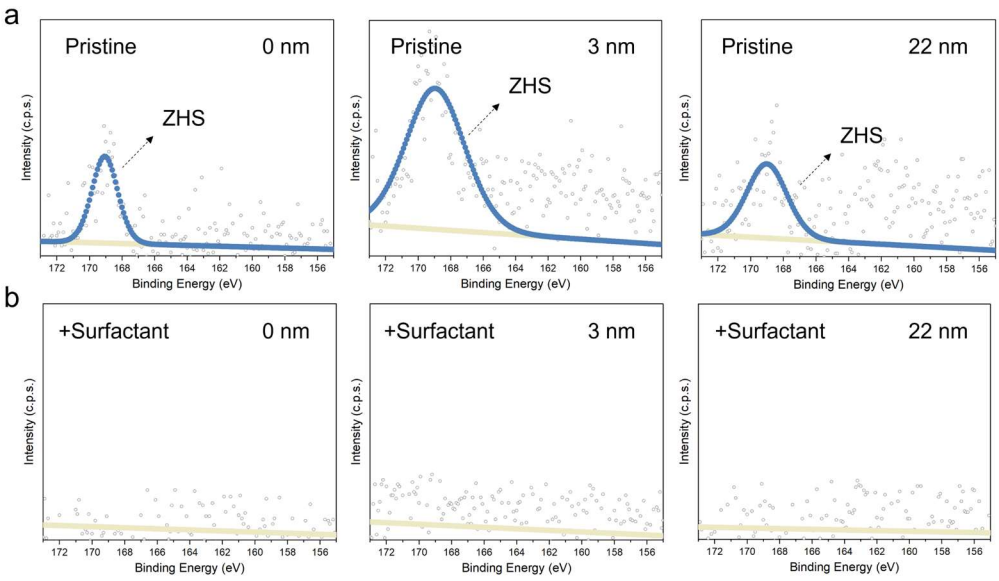

Supplementary Fig. 9.

In-depth XPS analysis (S 2p spectra) of interphase components of Zn formed in the DEFBs using the pristine electrolyte (a) or surfactant electrolyte (b) after 10 cycles (charging at 2.3 V up to 0.5 mAh/cm² and discharging at 5 mA/cm² down to 1 V). Sputtering rate is ~1 nm/min based on SiO_2.

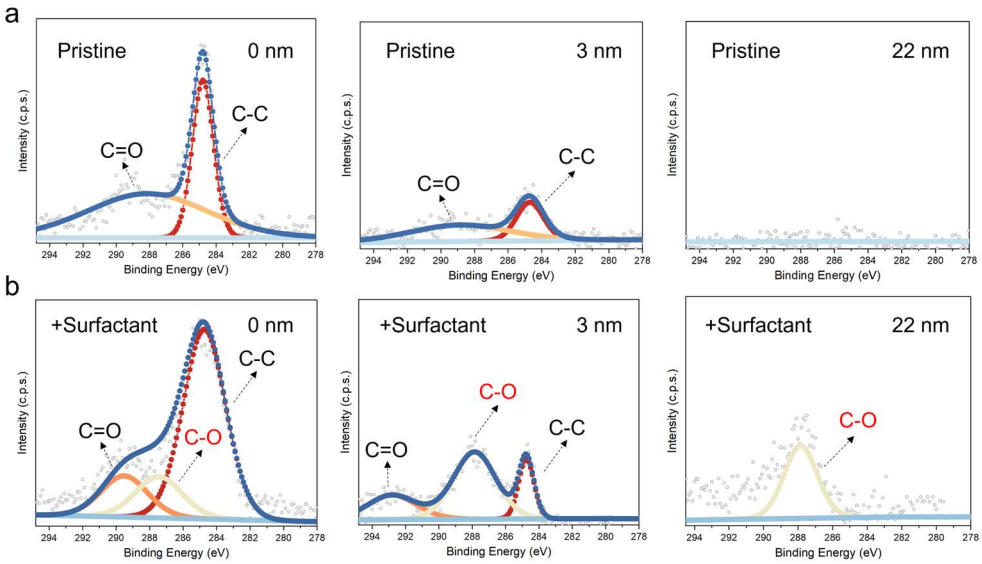

Supplementary Fig. 10.

In-depth XPS analysis (C 1s spectra) of interphase components of Zn formed in the DEFBs using the pristine electrolyte (a) or surfactant electrolyte (b) after 10 cycles (charging at 2.3 V up to 0.5 mAh/cm² and discharging at 5 mA/cm² down to 1 V). Sputtering rate is ~1 nm/min based on SiO_2. The C=O signal may originate from carbonates produced by trace amounts of CO_2 dissolved in the electrolyte[1].

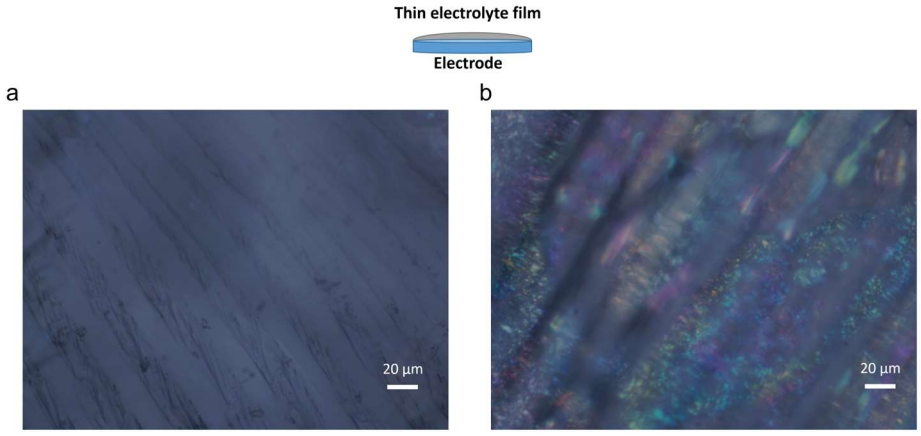

Supplementary Fig. 11.

POM images of Zn surface formed in the DEFBs using the pristine electrolyte (a) or surfactant electrolyte (b) after 10 cycles (charging at 2.3 V up to 0.5 mAh/cm² and discharging at 5 mA/cm² down to 1 V), captured under reduced light intensity. The dark images more clearly show that the colored (b) image has a liquid crystal phase.

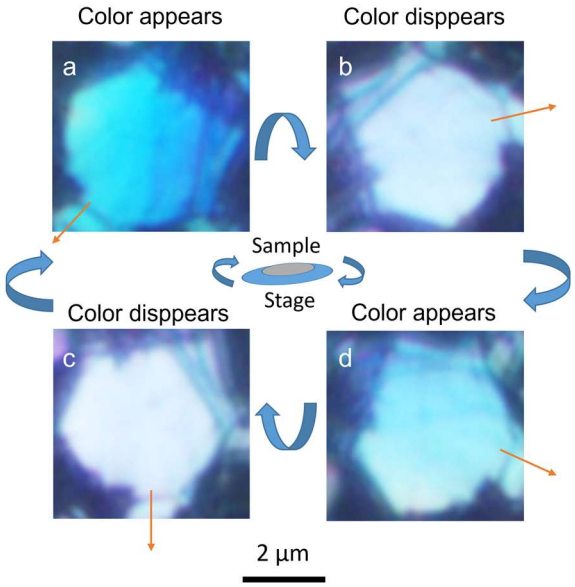

Supplementary Fig. 12.

POM images of Zn surface formed in the DEFB using the surfactant electrolyte after 10 cycles (Extinction observation[2]). In order to obtain a clear POM image of the surface of (002) plane, we increased the deposition capacity (charging at 2.3 V up to 5 mAh/cm² and discharging at 15 mA/cm² down to 1 V) to obtain a larger (002) plane. The orange arrow represents the reference position. In crossed polarized illumination, isotropic materials can be easily distinguished from anisotropic materials as they remain permanently in extinction (remain no color change) when the stage is rotated through 360 degrees.

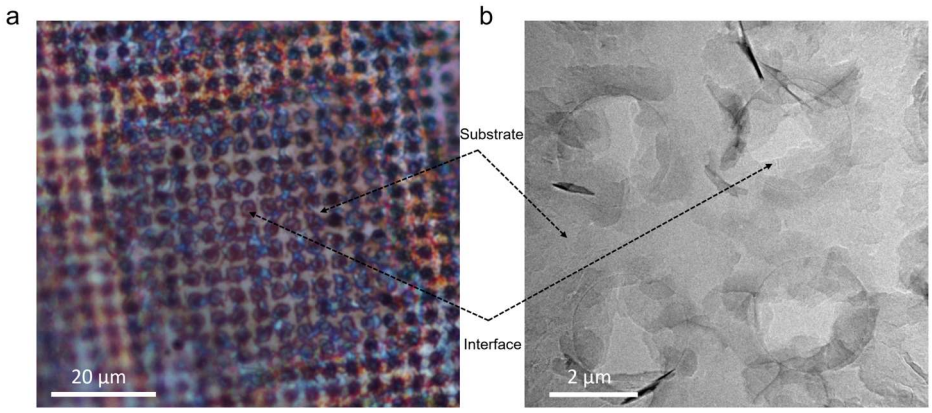

Supplementary Fig. 13.

POM image of Zn deposited in the DEFB using the surfactant electrolyte and porous Cu grid mesh (a) and its further Cryo-TEM investigation (b). POM image confirms the formation of liquid crystal interphase on Zn surface.

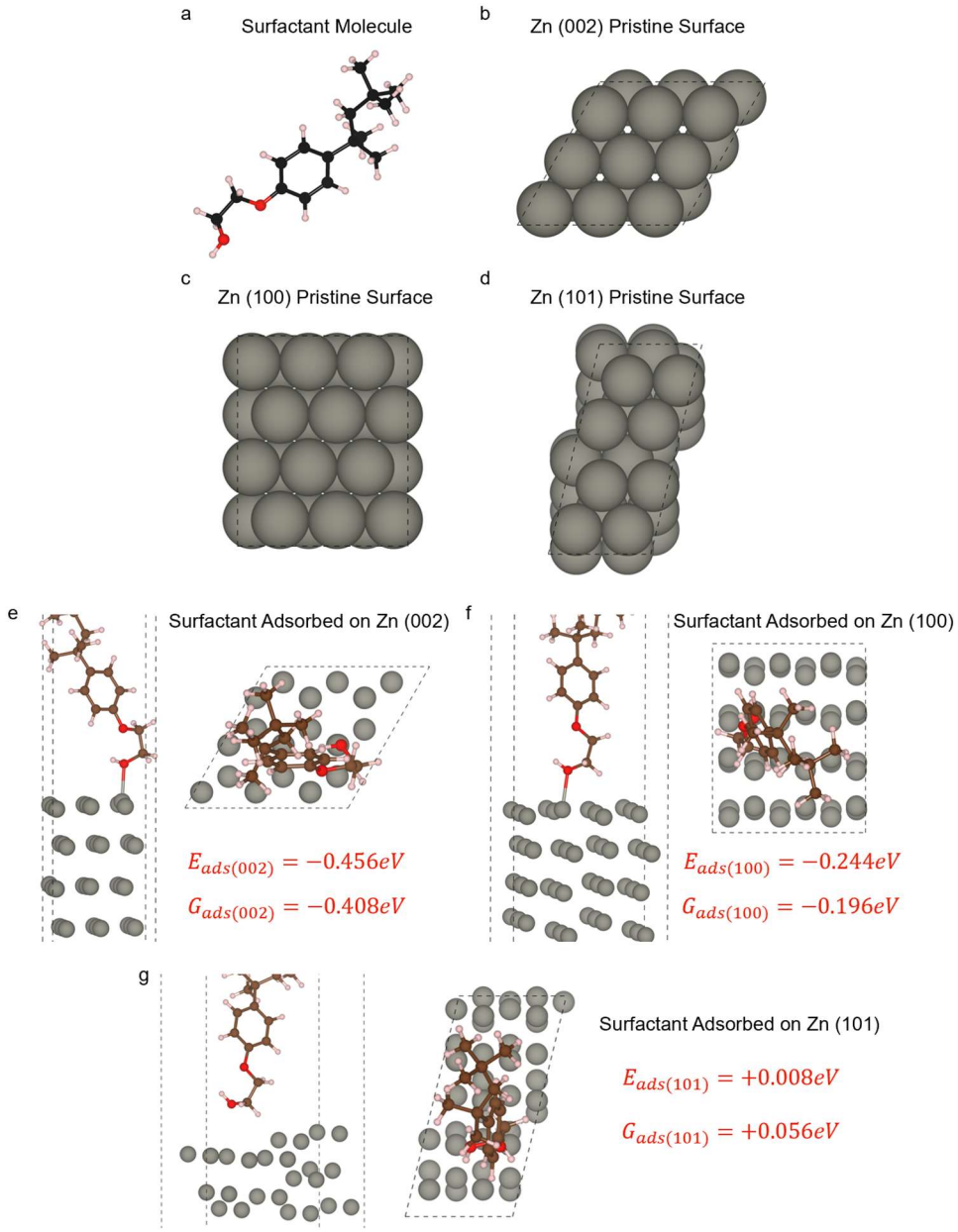

Supplementary Fig. 14.

DFT calculations of surfactant adsorption on low-index Zn surfaces. (a-d) Models of the surfactant molecule (simplified to $C_{14}H_{21}O(C_2H_4OH)$ to keep calculations tractable), Zn (002), Zn (100), and Zn (101). (e-g) Adsorption of the surfactant molecule on Zn (002) (e), Zn (100) (f), and Zn (101) (g). All of the adsorption model diagrams include top and side views. Brown: Carbon; White: Hydrogen; Red: Oxygen; Grey: Zinc. DFT-computed electronic energies (E_{ads}) and free energies (G_{ads}, including zero-point and vibrational energies, as well as entropy) are shown for each adsorption reaction. Surfactant adsorption can be as the driving force for surfactant aggregation on Zn.

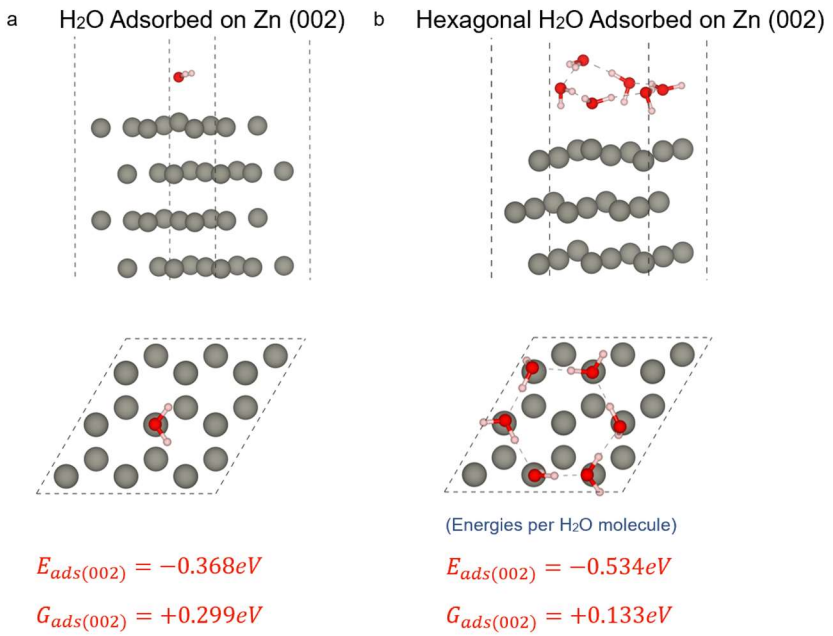

Supplementary Fig. 15.

DFT calculations reveal only a weak interaction between water and Zn (002). (a) Stability of a single physisorbed H_2O molecule, (b) Stability of a hexagonal water overlayer. Each of the diagrams include side and top views. White: Hydrogen; Red: Oxygen; Grey: Zinc. DFT-computed electronic energies (E_{ads}) and free energies (G_{ads}, including zero-point and vibrational energies, as well as entropy) are shown for each reaction.

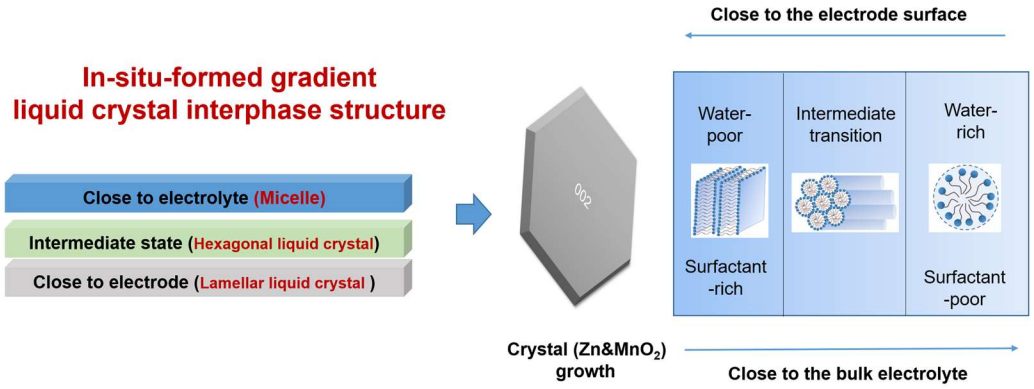

Supplementary Fig. 16.

Schematic illustrating the in situ formed gradient liquid crystal interphase structure.

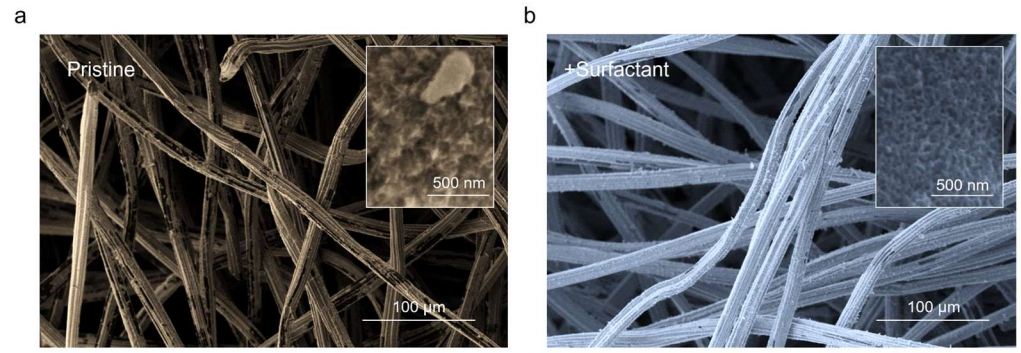

Supplementary Fig. 17.
SEM images of deposited MnO_2 formed in the DEFBs using the pristine electrolyte (a) or surfactant electrolyte (b) after 10 cycles (charging at 2.3 V up to 0.5 mAh/cm² and discharging at 5 mA/cm² down to 1 V). Inset: the zoom-in SEM images.

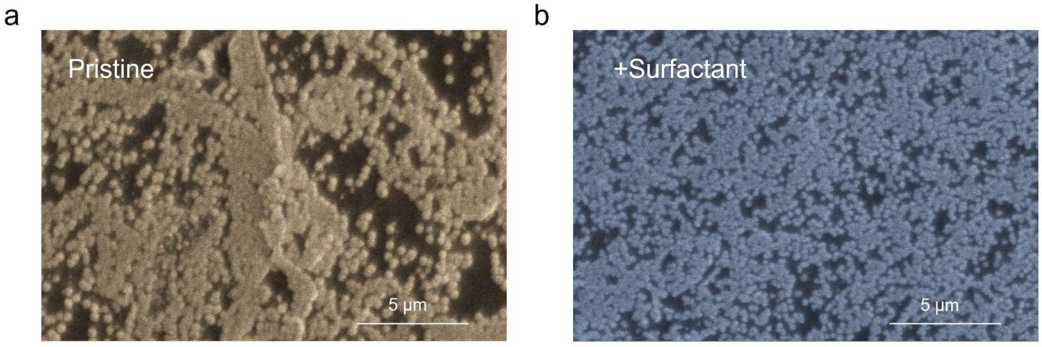

Supplementary Fig. 18.
SEM images of MnO_2 formed in the DEFBs using the pristine electrolyte (a) or surfactant electrolyte (b). Note the graphite foil (not felt) is used in this experiment. Deposited capacity is set as 50 µAh to investigate the nucleation process (constant voltage of 2.3 V). The pristine electrolyte results in uneven nucleation, while the surfactant electrolyte can promote uniform nucleation.

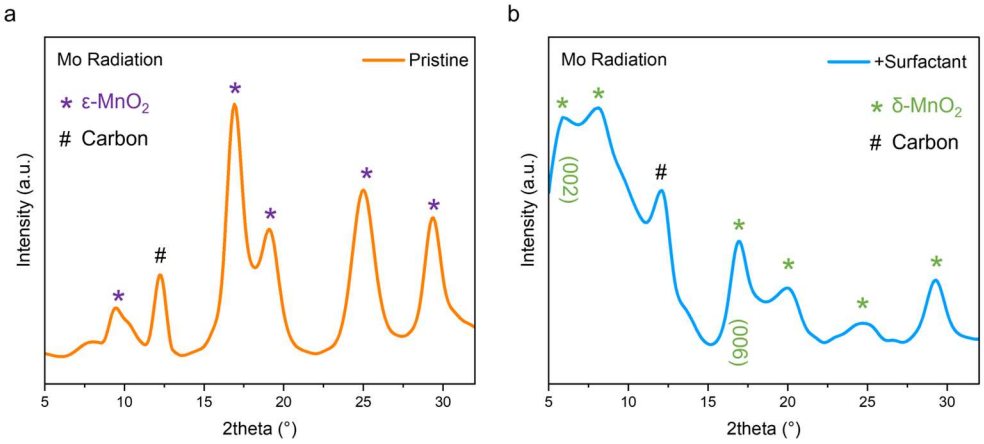

Supplementary Fig. 19.

XRD analysis (Mo radiation) of deposited MnO_2 on graphitic carbon using the pristine electrolyte (a) or surfactant electrolyte (b). The reference pdf card numbers are 00-056-0159 (graphitic carbon), 00-030-0820 (ε-MnO_2) and 00-018-0802 (δ-MnO_2), respectively. The positions and relative intensities of the peaks are different but since some of the peak positions of the two are repeated, it is more likely that both are polycrystalline, but have different main phase components.

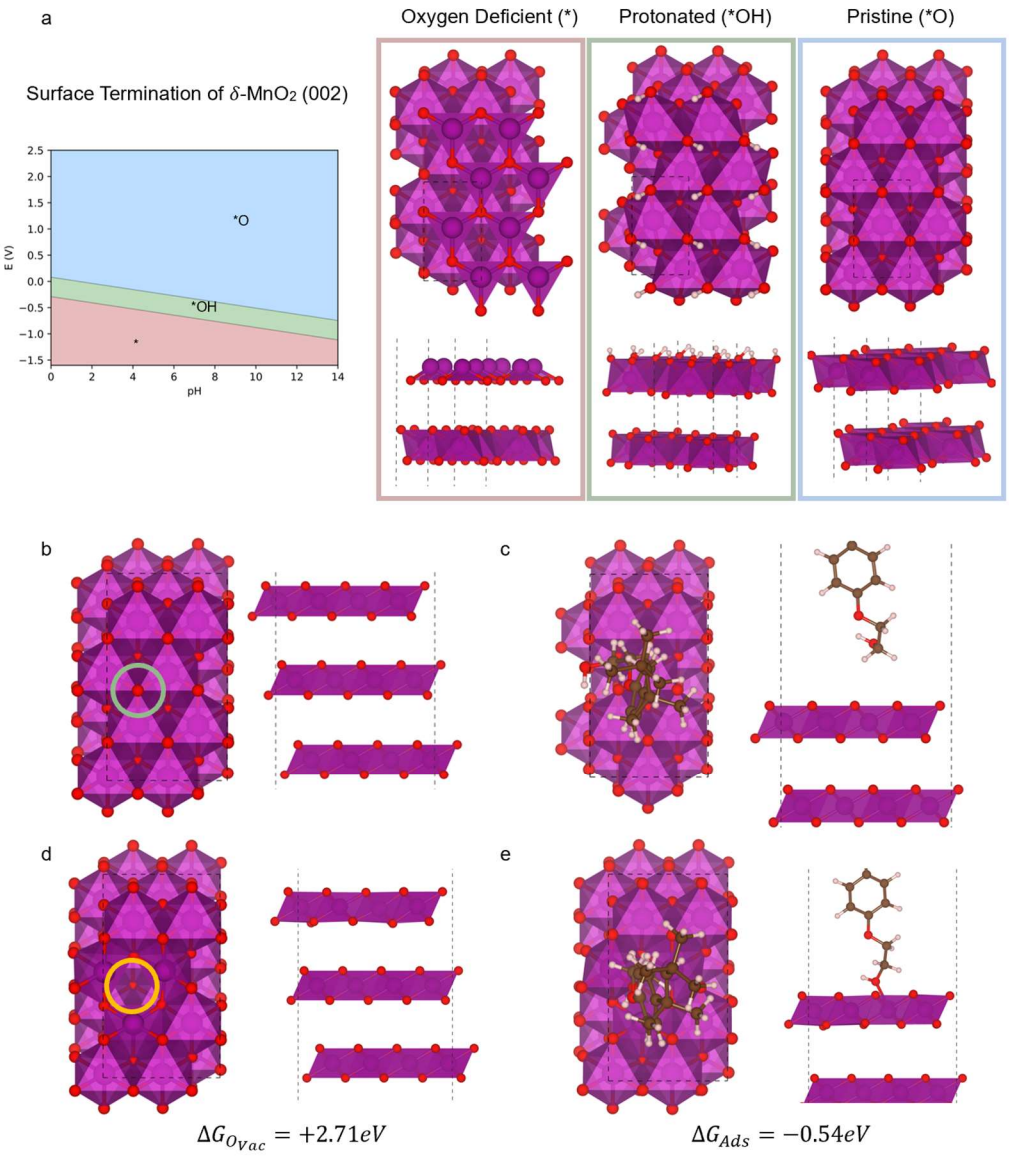

Supplementary Fig. 20.

(a) Surface Pourbaix diagram of δ-MnO_2 (002) showing the most stable surface terminations as a function of pH and voltage. The O* termination is stable under all battery-relevant conditions. Dashed lines show overpotentials for formation of O vacancies via oxidation and reduction of lattice O. (b) DFT calculations showing surfactant does not adsorb on O*-terminated δ-MnO_2 (002) in the absence of a surface O vacancy. Electrostatic repulsion between the surfactant OH group and the surface O in MnO_2 prevents bond formation. (c) In the presence of O vacancies, surfactant adsorption is downhill in free energy. (d) Reaction coordinate diagram of O vacancy formation via lattice O oxidation. This reaction is only favorable at voltages > 3.27 V vs. reversible hydrogen electrode (RHE) since the *OOH intermediate is highly unstable. (e) Reaction coordinate diagram of O vacancy formation via lattice O reduction, which is only favorable at voltages < −0.14 V vs. RHE since desorption of *OH is unfavorable.

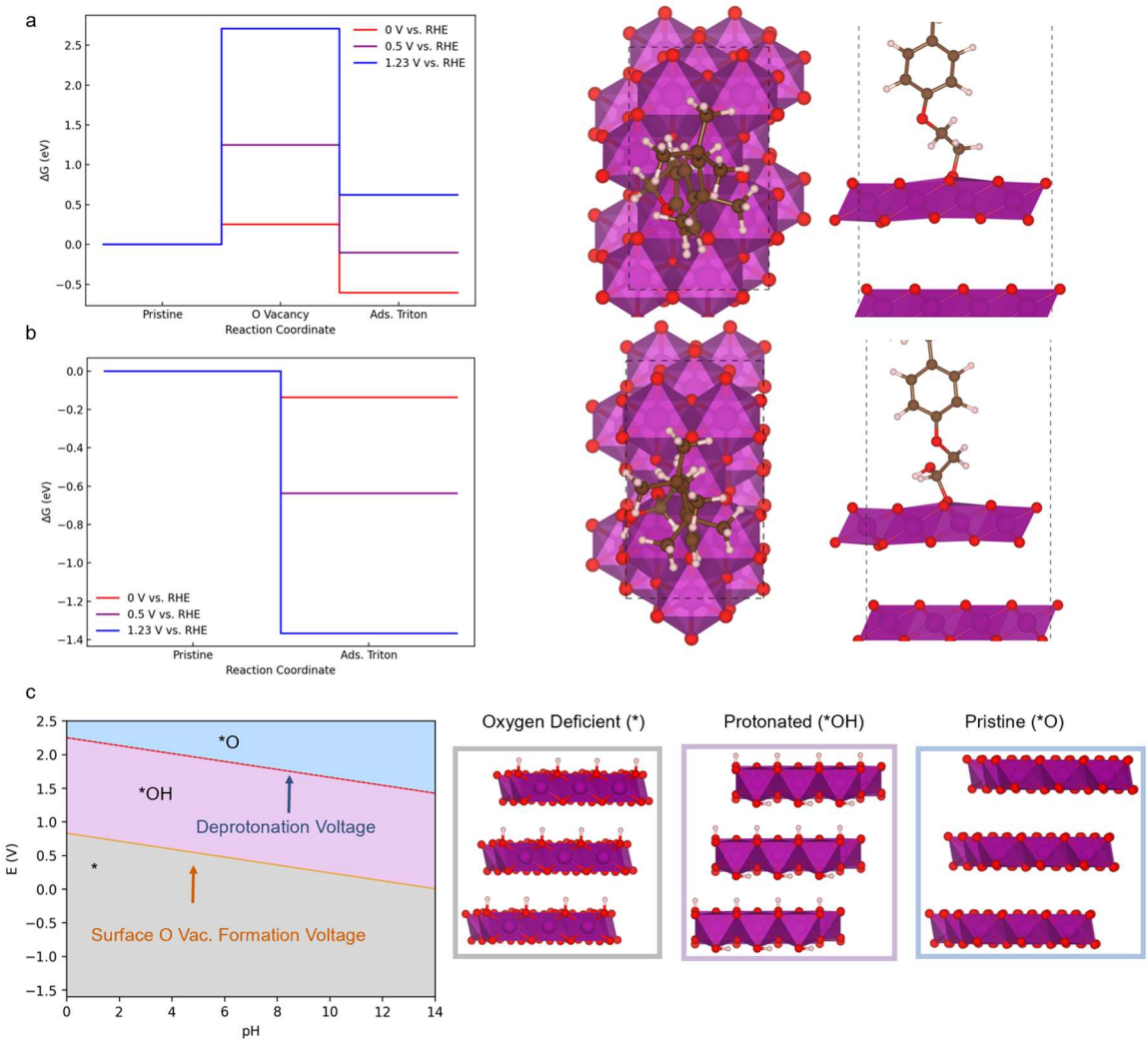

Supplementary Fig. 21.

(a) Reaction coordinate diagram and schematics showing favorable oxidative adsorption mechanism on δ-MnO_2 (002) (surfactant is oxidized, proton is released from C-H bond, surfactant adsorbs via C-O bond). (b) Reaction coordinate diagram and schematics of unfavorable non-oxidative adsorption mechanism, requiring the presence of a surface O vacancy (O_2 is evolved leaving behind surface O vacancy, surfactant adsorbs onto O vacancy site) (see Supplementary Fig. 20). (c) Surface Pourbaix diagram of δ-MnO_2 (100) showing the most stable surface terminations as a function of pH and voltage. *OH termination is the most stable under battery-relevant conditions. Surfactant adsorption on this facet is unfavorable because it requires deprotonation of reactive oxygen, which is unfavorable below 2 V vs. RHE (dashed line).

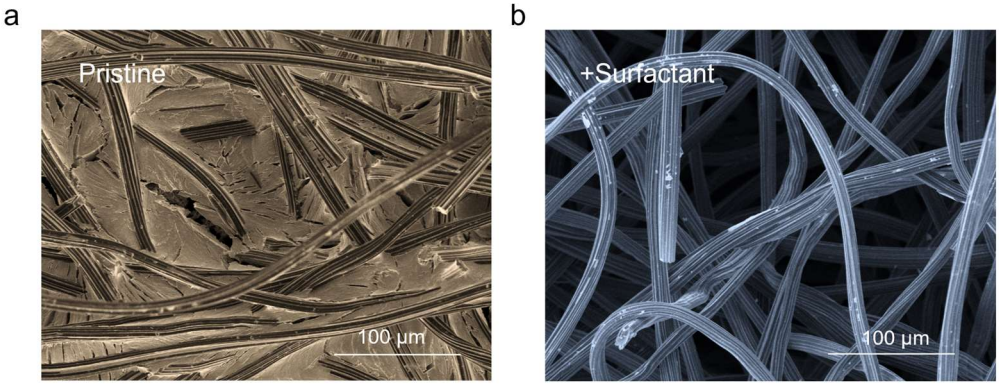

Supplementary Fig. 22.

SEM images of MnO_2 stripping in the DEFBs using the pristine electrolyte (a) or surfactant electrolyte (b) after 10 cycles (charging at 2.3 V up to 0.5 mAh/cm² and discharging at 5 mA/cm² down to 1 V). In the pristine electrolyte, a substantial residue (ZHS) is observed on the carbon felt surface following MnO_2 stripping. Conversely, the use of surfactant electrolyte results in a relatively clean carbon felt surface.

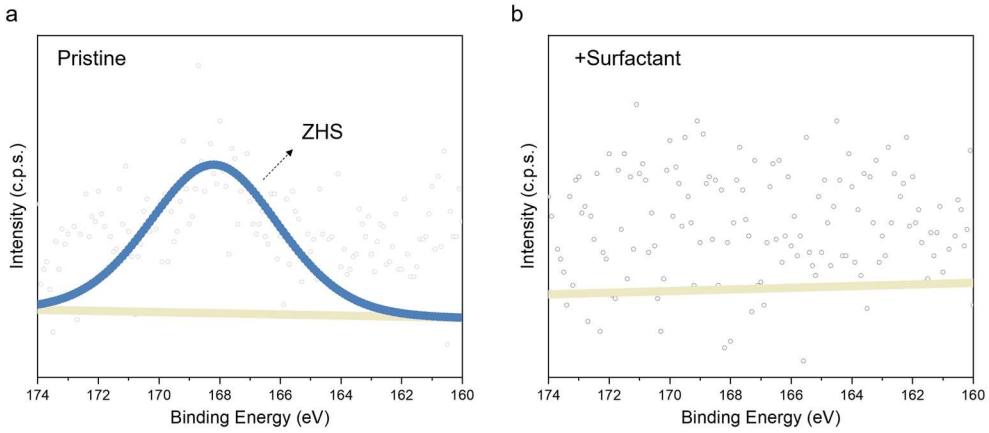

Supplementary Fig. 23.

XPS analysis (S 2p spectra) of interphase components of MnO_2 formed in the DEFBs using the pristine electrolyte (a) or surfactant electrolyte (b) after 10 cycles (charging at 2.3 V up to 0.5 mAh/cm² and discharging at 5 mA/cm² down to 1 V).

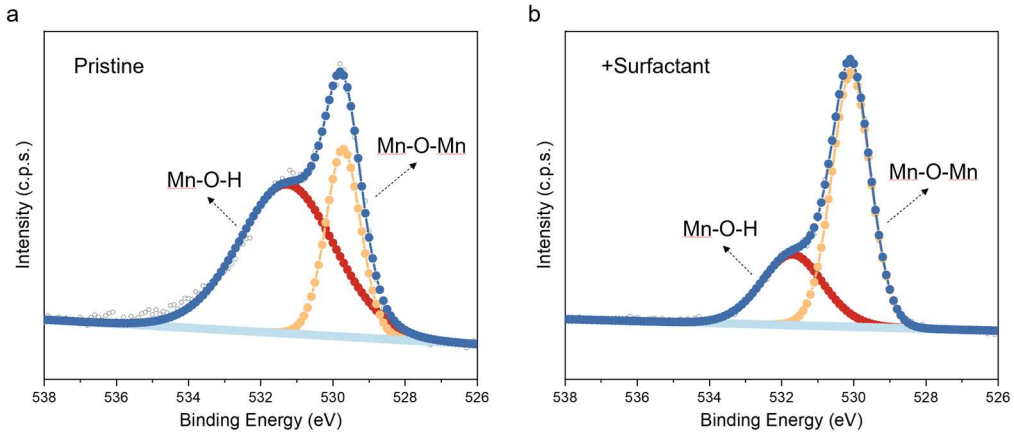

Supplementary Fig. 24.

XPS analysis (O 1s spectra) of interphase components of MnO_2 formed in the DEFBs using the pristine electrolyte (a) or surfactant electrolyte (b) after 10 cycles (charging at 2.3 V up to 0.5 mAh/cm² and discharging at 5 mA/cm² down to 1 V). The signal of Mn-O-H (MnOOH) can reflect the amount of trivalent manganese (the dissolved Mn^{3+} easily results in a loss of active species)[3].

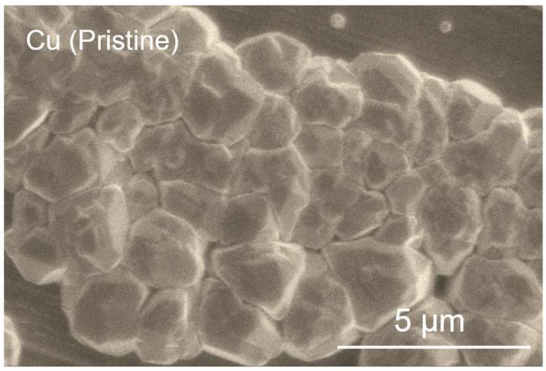

Supplementary Fig. 25.

SEM images of Cu formed in the DEFB (Cu/MnO_2) using the pristine electrolyte after 10 cycles (charging at 1.3 V up to 0.5 mAh/cm² and discharging at 5 mA/cm² down to 1 V).

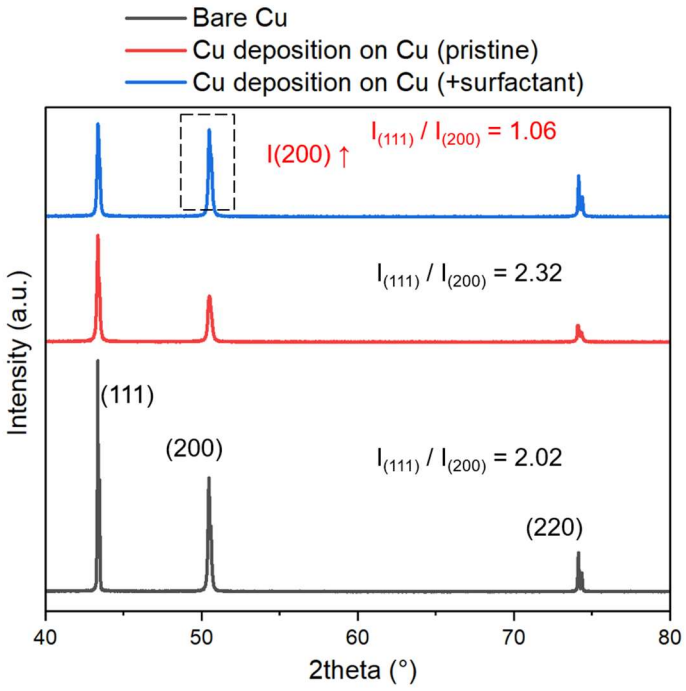

Supplementary Fig. 26.

XRD analysis of bare Cu, and Cu formed in the DEFBs (Cu/MnO_2) using the pristine electrolyte or surfactant electrolyte after 10 cycles.

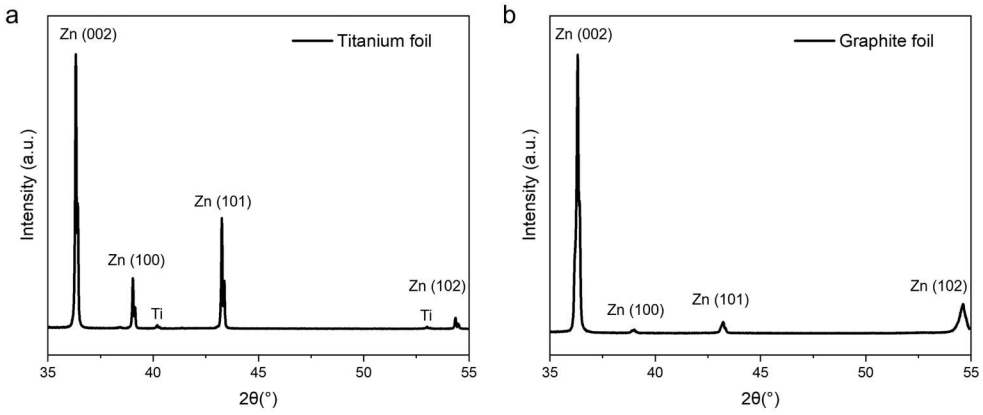

Supplementary Fig. 27.

XRD analysis of Zn formed in the DEFBs using the surfactant electrolyte after 10 cycles (charging at 2.3 V up to 0.5 mAh/cm² and discharging at 5 mA/cm² down to 1 V) with Ti foil (a) or graphite foil (b) as the substrate, respectively. Note that graphite seems to enable more obvious preferred orientation of (002) plane, possibly caused by that the native preferred orientation of (002) in graphite foil facilitates epitaxy growth[4].

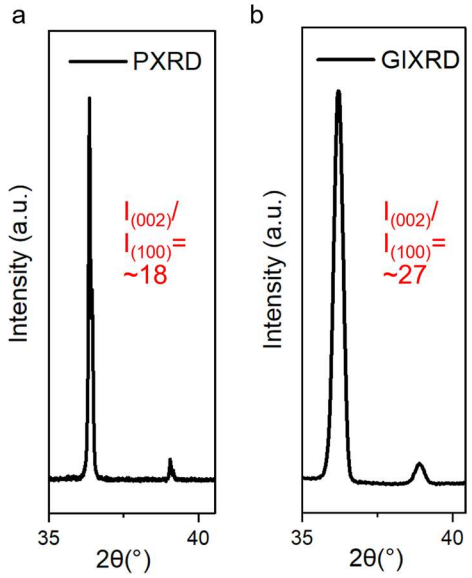

Supplementary Fig. 28.

Powder XRD (PXRD) and grazing incidence XRD (GIXRD) analysis of Zn formed in the DEFBs using the surfactant electrolyte with Cu foil as the substrates, respectively. We used GIXRD to obtain more surface information. Here we use a very small omega degree to perform the GIXRD. For PXRD, the intensity ratio of the (002) crystal plane to the (100) crystal plane is 18, but for GIXRD, the intensity ratio of the (002) crystal plane to the (100) crystal plane is 27. The closer to the interface, the more obvious the preferred orientation. Thus, there is an obvious interface influence after adding surfactant.

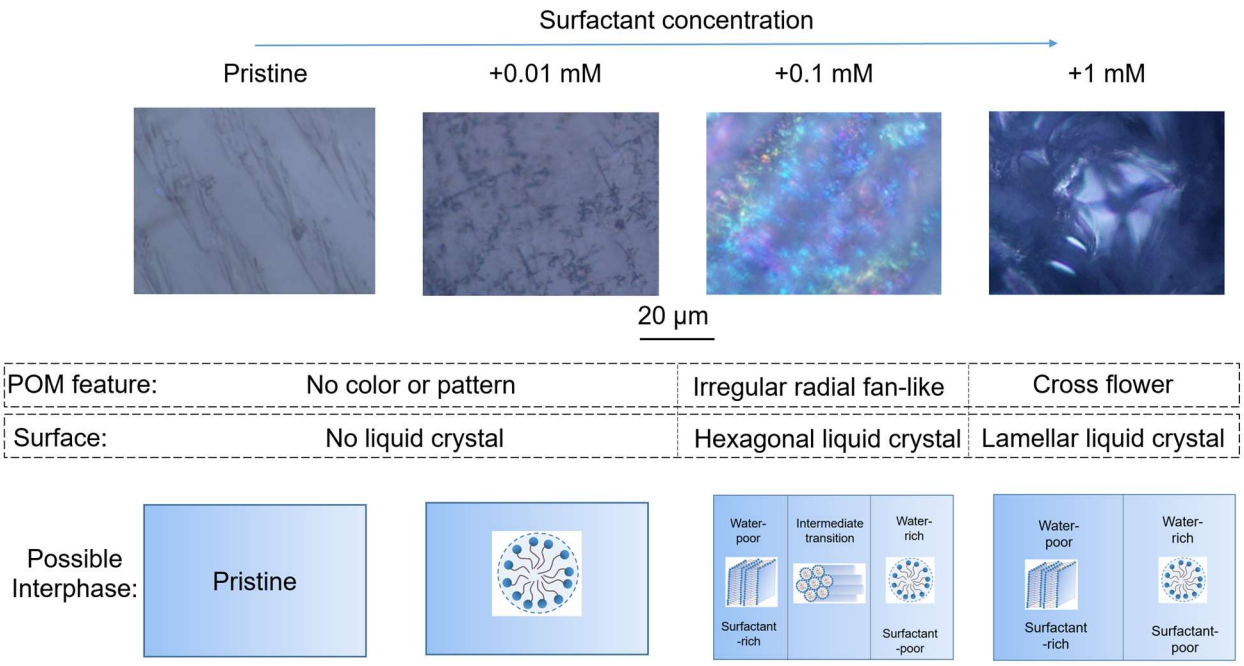

Supplementary Fig. 29.

POM images of Zn surface formed in the DEFBs using different electrolytes after 10 cycles (charging at 2.3 V up to 0.5 mAh/cm² and discharging at 5 mA/cm² down to 1 V) and schematic diagrams of their possible interphases[5,6].

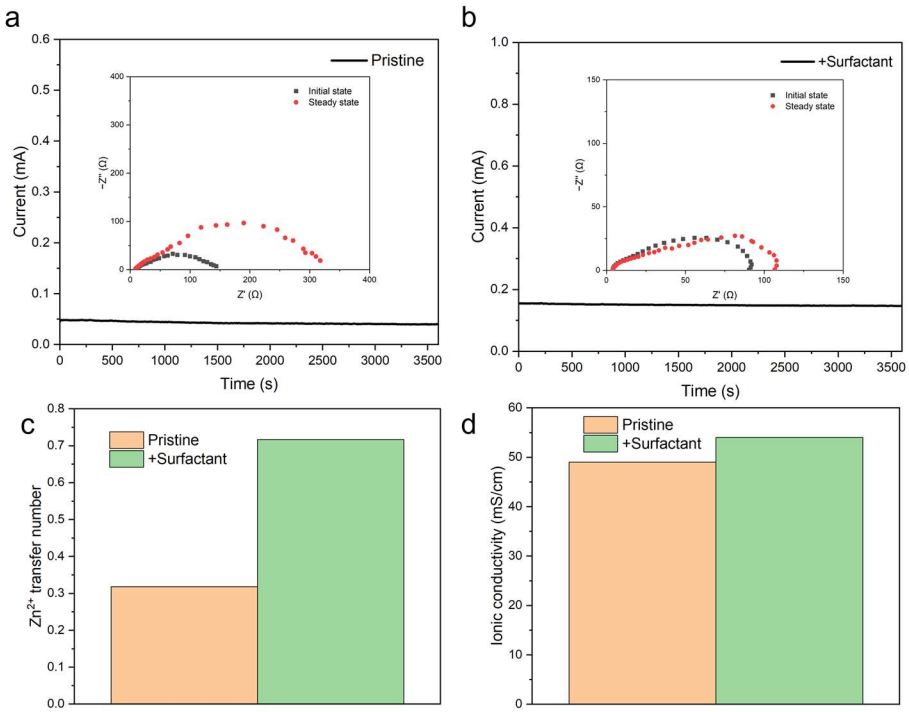

Supplementary Fig. 30.

Current-time plots of Zn||Zn symmetric cells in the (a) pristine and (b) surfactant electrolytes after polarization at a constant potential (10 mV) for 3600 s. The insets present the impedance spectra before and after polarization. (c) Zn^{2+} transference number in the pristine and surfactant electrolytes. (b) Ionic conductivity tests for two electrolytes (Pristine: 1 M $ZnSO_4$; Optimized: +0.1 mM surfactant).

Regarding the ion conductivity of this liquid crystal interphase layer, it is challenging to obtain precise measurements directly because the liquid crystal phase is formed in situ and exhibits a gradient structure, making it difficult to isolate and position between two blocking electrodes. Therefore, to preserve the integrity of this interphase, we employ non-invasive electrochemical impedance spectroscopy (EIS) to further obtain its kinetics parameters. The Zn^{2+} transference number was first evaluated using a Zn||Zn symmetric cell with chronoamperometry and impedance tests, as shown in Supplementary Figs. 30a and 30b. After calculation (the calculation method refers to previous literature[7]), the Zn^{2+} transference number in the surfactant electrolyte (~0.72) is significantly higher than that in the pristine electrolyte (~0.31) in Supplementary Fig. 30c. This illustrates that the liquid crystal interphase acts as a near-single conducting Zn^{2+} SEI[8]. The liquid crystal layer facilitates the transport of cations while hindering anion movement. A high transference number also indicates that the liquid crystal layer on the Zn electrode can suppress Zn dendrite formation by improving the concentration gradient at the interface[9].

We further tested the ionic conductivity of the two liquid electrolytes and found that the surfactant electrolyte had a slightly higher ionic conductivity (~53.9 mS/cm) than that of pristine one (~49.1 mS/cm) in Supplementary Fig. 30d, which may be due to the improvement of the solvation structure brought about by the micelle structure[10].

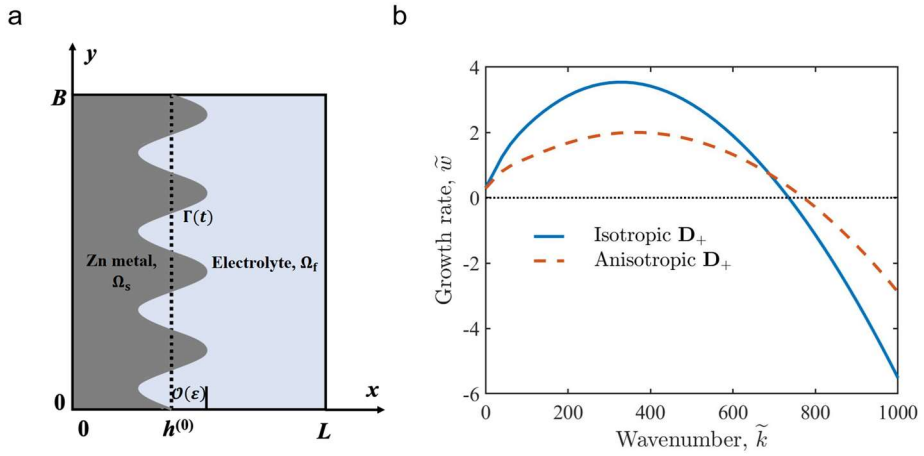

Supplementary Fig. 31.

Modeling of Zn dendrite initiation under the liquid crystal interphase. (a) Schematic representation of a two-dimensional computational domain $\Omega = \Omega_s \cup \Omega_e$. The interface between the Zn metal, Ω_s, and electrolyte, Ω_f, is denoted by Γ. A negative electrostatic potential, φ_e, is maintained on the Zn metal electrode surface, $\Gamma(t)$, at all time t; the electric potential at the outer edge of the electrolyte ($x = L$) is fixed at 0. The initial concentration of Zn cations, Zn^{2+}, in the binary dilute electrolyte electrolyte is c_0. (b) Dispersion relations $\tilde{w} = \tilde{w}(\tilde{k})$ computed without liquid crystal (constant isotropic diffusion coefficients) or with liquid crystal (constant anisotropic diffusion coefficients).

The aggregation of surfactant induces local liquid-crystal with anisotropic diffusion coefficients where $D_{xx}^{\pm}$ and $D_{yy}^{\pm}$ are the constant cation/anion diffusion coefficient components in the principal x and y directions. The impact of anisotropic ion diffusion in the liquid-crystal is investigated through a linear stability analysis[11,12]. We employ the Poisson-Nernst-Planck equations coupled with the Butler-Volmer kinetics to describe electrodeposition. Our two-dimensional computation domain is shown in Fig. a. Fig. b exhibits the dispersion relations $\tilde{w} = \tilde{w}(\tilde{k})$ for $\phi e = -2.3$ V corresponding to two scenarios: one with constant isotropic diffusion coefficients, $D_{yy}^{\pm} = D_{xx}^{\pm} = D^{ref}$ (absence of liquid crystal), and the other with constant anisotropic diffusion coefficients, where with $D_{xx}^{+} \neq D_{yy}^{+}$, when liquid crystal forms. Regarding the Zn^{2+} diffusivity within the liquid crystal, we utilize the transport properties associated with the hexagonal phase[13] instead of treating the electrolyte as composite materials[14,15]. In the presence of anisotropic diffusion due to liquid crystal formation, the maximum growth rate $\tilde{w}_{max}$ decreases by approximately 50%. This change indicates that the emergence of liquid crystal and the anisotropy in Zn^{2+} diffusion contribute to the suppression of dendrite growth. Over a broad range of wavenumbers ($\tilde{k}$ ranging from 100 to 600), anisotropic diffusion leads to significantly smaller growth rates compared to the isotropic diffusion case. However, within a confined wavenumber range ($\tilde{k}$ ranging from 700 to 750), the growth rate associated with isotropic diffusion coefficients slightly surpasses that of anisotropic diffusion coefficients. This discrepancy is attributed to the higher diffusivity of Zn^{2+} in the liquid electrolyte relative to its diffusivity in the liquid crystal. Our analysis underscores the potential for mitigating dendrite growth by enhancing Zn^{2+} diffusion perpendicular to the Zn metal surface. This would alleviate dendrite-related issues in aqueous Zn batteries by reducing growth rates through the formation of anisotropic diffusion due to the presence of liquid crystal.

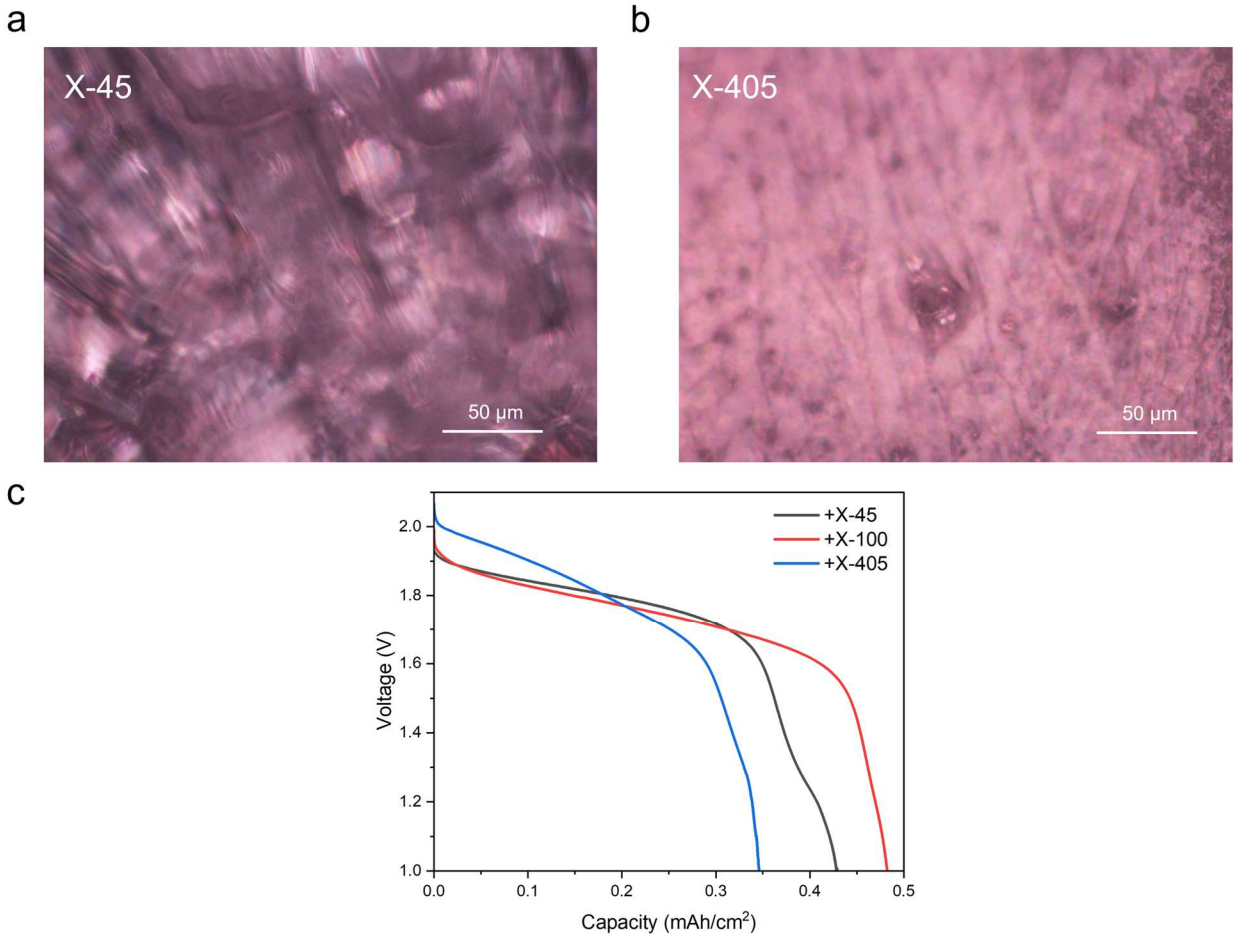

Supplementary Fig. 32.

(a,b) POM images formed in Zn surface using the X-45-based electrolyte (a) or X-405-based electrolyte (b). (c) Electrochemical tests using the electrolytes with different kinds of surfactants (charging at 2.3 V up to 0.5 mAh/cm² and discharging at 5 mA/cm² down to 1 V).

Besides the surfactant (t-Oct-C_6H_4-$(OCH_2CH_2)_n$OH, n=9-10) used in our work (abbreviated as X-100), we further purchased the surfactant (t-Oct-C_6H_4-$(OCH_2CH_2)_n$OH, n=~5) (abbreviated as X-45) and (t-Oct-C_6H_4-$(OCH_2CH_2)_n$OH, n=~40) (abbreviated as X-405) for further investigation. Similarly, both surfactants were mixed into the pristine electrolyte at a concentration of 0.1 mM, respectively, and zinc deposition experiments were conducted. The liquid crystal phases on the surface were further studied using POM.

As shown in Supplementary Fig. 32a, the X-45 sample exhibited partial radial (rainbow-like and fan-like) interference colors, similar to the X-100 sample (Fig. 3d in the main text), but not as uniformly covered as X-100. The X-405 sample showed almost no interference colors (Supplementary Fig. 32b), indicating the absence of a liquid crystal phase. Note that the difference in background color of the POM images shown in the article mainly comes from the adjustment of instrument parameters.

Thus, the chain length (n) of the surfactant (t-Oct-C_6H_4-$(OCH_2CH_2)_nOH$) plays a crucial role in determining the properties and behavior of the liquid crystal interphase. Here are some thoughts on how the chain length affects the liquid crystal interface and the balance required:

- The length of the ethylene oxide (EO) chain (n) affects the hydrophilic-lipophilic balance of the surfactant.[16]
- For shorter chains ($n < 5$), such as X-45, the surfactant becomes more hydrophobic, leading to less effective hydration and weaker interaction with the aqueous phase, resulting in poorly formed liquid crystal phases.
- For longer chains ($n > 15$), such as X-405, the surfactant becomes more hydrophilic, which can enhance solubility in water but may disrupt the formation of well-ordered liquid crystal structures due to excessive hydration and steric hindrance.
- A chain length of 9-10 EO, such as X-100, units provide an optimal balance between hydrophilicity and lipophilicity, facilitating the formation of stable liquid crystal phases.

We further tested their electrochemical performance and found that the ranking of performance is as follows: X-100 exhibited the best performance, followed by X-45, and then X-405 (Supplementary Fig. 32c). This demonstrates that a stable and uniform gradient liquid crystal phase is crucial for achieving good electrochemical performance in DEFBs.

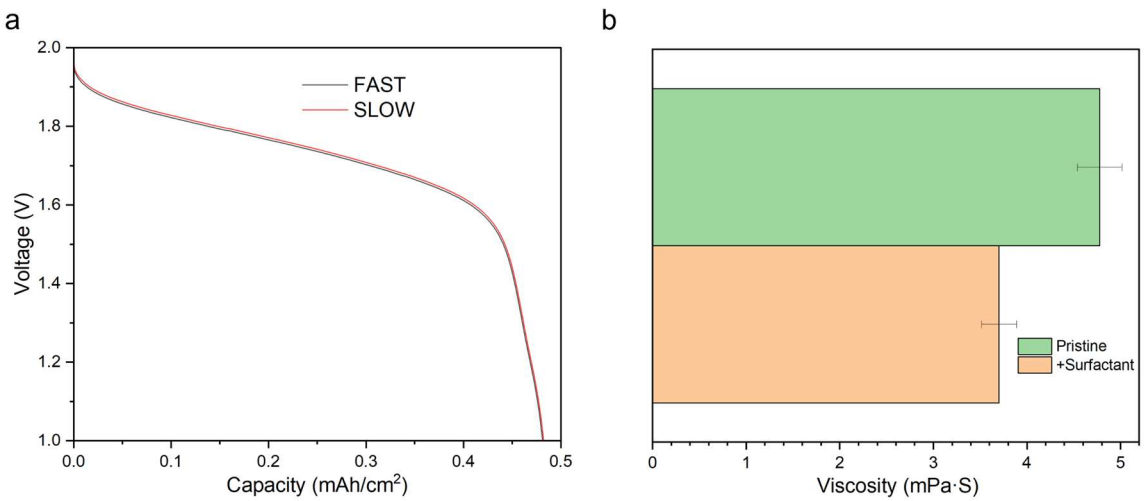

Supplementary Fig. 33.

(a) Electrochemical tests of DEFB using the surfactant electrolyte for different resting time. (b) Viscosity tests for the pristine and surfactant electrolytes.

A finite waiting period is indeed required to allow the surfactant to wet the current collector before deposition/stripping occurs, but this time can be very short. Here are the details:

To assess the influence of wetting time, we designed additional tests. For DEFB cell assembly, the fastest assembly time from electrolyte injection to sealing and testing is around 1-2 minutes, labeled as "FAST". We also tested a waiting period of 8 hours (long resting time after assembly), labeled as "SLOW". As shown in Supplementary Fig. 33a, the performance comparison shows that the discharge curves of both FAST and SLOW setups are nearly identical, with the SLOW setup showing slightly better performance, likely due to the additional time allowing the separator to be fully wetted. Previous literature indicates that surfactant adsorption and wetting can often occur within seconds[17-19].

Additionally, we measured the viscosity of both electrolytes and found that the surfactant electrolyte has lower viscosity (~3.7 mPa·s) than the pristine one (~4.8 mPa·s) in Supplementary Fig. 33b. This is attributed to the surfactant's ability to reduce surface tension, aiding in the rapid wetting of the entire cell and enhancing kinetics. The error bar (standard deviation) of viscosity data was obtained by five samples from different batches. The average used is the mean value. The data of this Figure are presented as the mean values ± standard error of the mean.

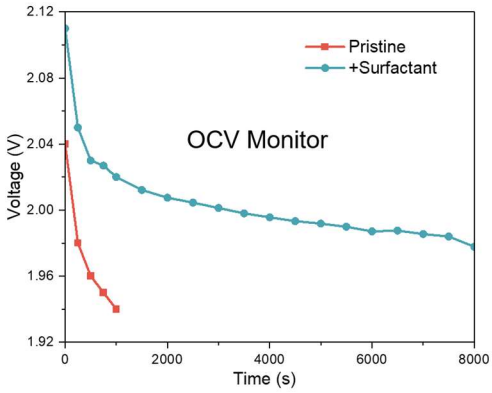

Supplementary Fig. 34.

Open circuit voltage monitoring (long-term resting) of the DEFBs with fully charged state (2.3 V). Our study indicates that the liquid crystal interphase can play a significant role in mitigating proton crossover.

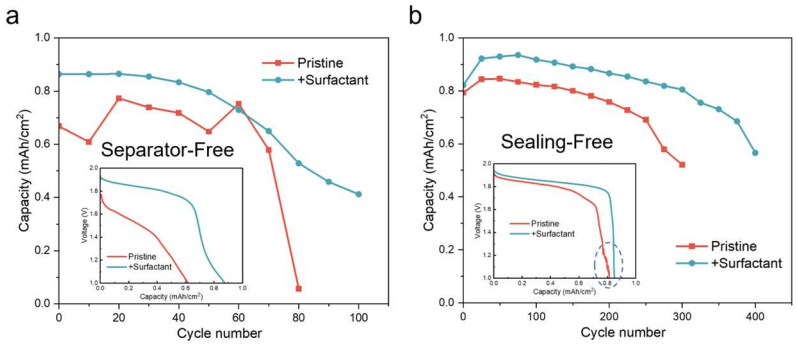

Supplementary Fig. 35.

Cycling tests using the pristine electrolyte or surfactant electrolyte (charging at 2.3 V up to 1 mAh/cm² and discharging at 5 mA/cm² down to 1 V) without separator (a) or sealing component (b). Inset: the 10th curve.

The separators in aqueous batteries are typically made of glass fibers, which are relatively thick and costly. Designing batteries without separators can enhance energy density while reducing costs. However, this presents a challenge as it makes the cathode or anode more susceptible to micro-short circuits. Dead Zn and MnO_2, which lose electrical connection with the base, can float in the electrolyte, potentially causing a short circuit. Therefore, DEFBs using the pristine electrolyte exhibit unstable CE (Supplementary Fig. 35). The in situ formed liquid crystal interphase can mitigate the production of inactive deposits and protect the active deposits, thus prolonging the lifespan.

Sealing-free design in aqueous batteries is a double-edged sword[20]; it can simplify the battery structure further, allowing for the addition of water inlets to replenish the electrolyte and facilitate the release of generated gases. However, due to the easy evaporation of water, the electrolyte might dry up quickly, potentially manifesting as fluctuations at the end of discharge. Surfactant molecules and the liquid crystal interphase likely also have a fluid retention function, thereby extending the DEFB's cycle life.

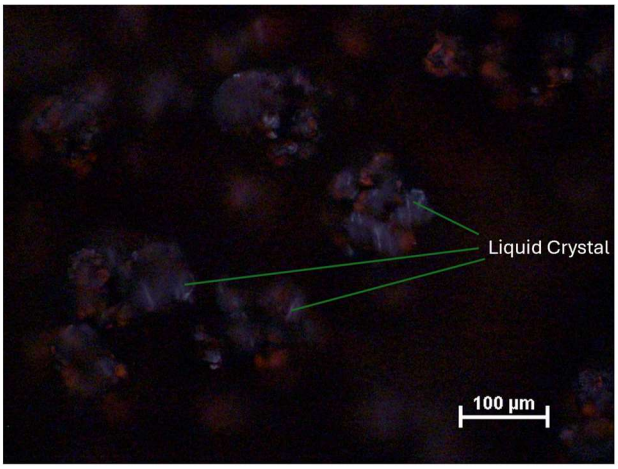

Supplementary Fig. 36.

POM image of Zn surface deposited in the sodium dodecyl benzene sulfonate (SDBS)-based surfactant electrolyte. We believe that the formation of a liquid crystal interphase may not be exclusive to the specific surfactant introduced in our work. For instance, we have also observed the in-situ formation of liquid crystal phases on the deposited Zn with a 0.25 mM SDBS additive in the 1 M $ZnSO_4$ electrolyte, as confirmed by POM in Supplementary Fig. 36. Although it is not uniform, it is obvious that the surface of zinc has birefringence even captured under reduced light intensity (showing colors that are not its own). This broadens the scope for further exploration and application of liquid crystal interphases in different electrochemical systems.

Supplementary Table 1.

Estimated energy density values based on different Zn/MnO_2 battery configurations.

	Specific capacity based on cathode (mAh/g)	Average voltage of full cell (V)	Anode mass (g)	Cathode mass (g)	Anode current collector mass (g)	Cathode current collector mass (g)	Separator mass (g)	Electrolyte mass (g)	Estimated energy density (Wh/kg)
Zn/MnO_2 batteries based on insertion-type cathode	290	1.44	23.76	3.44	2.10	5.24	2.03	2	37.3
Zn/MnO_2 batteries based on dual deposition	616	1.99	23.76	1.623	2.10	5.24	2.03	2	54.1
Zn/MnO_2 batteries based on dual deposition (cathode-free)	616	1.99	23.76	0	2.10	5.24	2.03	2	56.6
Zn/MnO_2 batteries based on dual deposition (anode-free)	616	1.99	0	1.623	2.10	5.24	2.03	2	153.2
Zn/MnO_2 batteries based on dual deposition (electrode-free)	616	1.99	0	0	2.10	5.24	2.03	2	175
Zn/MnO_2 batteries based on dual deposition (component-less)	616	1.99	0	0	2.10	5.24	0	2	213

The calculations were based on the areal capacity of 3 mAh/cm^2. Anode mass was calculated with 0.1 mm Zn foil. In order to ensure the good mechanical properties of anodes[21], we also consider the addition of Cu current collectors in the Zn metal-based batteries for our calculations.

Supplementary Note 1.

The reason we observed a gradient hexagonal-lamellar structure in our study can be attributed to two key factors: the lyotropic nature of the liquid crystals and the concentration gradient of the surfactant at the interface. Here's a detailed explanation with a focus on the growth dynamics of the in-situ formed liquid crystal phases:

Lyotropic Liquid Crystal Nature:

In our work, the liquid crystals formed are lyotropic[22], meaning their phase structure depends on the concentration of surfactant molecules. According to binary phase diagrams of water-surfactant systems[23]: Hexagonal Phase: Requires a lower concentration of surfactant molecules (~40-60%); Lamellar Phase: Requires a higher concentration of surfactant molecules (~60-80%).

Note that our electrochemically in-situ generated liquid crystal system is more complex, and these values may vary slightly. The observed gradient structure, transitioning from hexagonal to lamellar, reflects the changes in local surfactant concentration during the deposition process.

Surfactant Concentration Gradient at the Interface:

The distribution of surfactant molecules at the interface exhibits a concentration gradient, which is crucial for understanding the structural transitions. Here's how it works: (a) Near Zinc Surface: The concentration of surfactant molecules is higher due to adsorption, promoting the formation of lamellar structures; (b) Away from Zinc Surface: The concentration decreases, favoring the formation of hexagonal structures.

Growth Dynamics of the In-Situ Formed Liquid Crystal Phases:

The growth dynamics are driven by the changing concentration of surfactant molecules during the zinc deposition process:

- Initial Adsorption: Surfactant molecules adsorb onto the zinc surface, creating a thin layer (~5 nm). Our detailed DFT calculations (Supplementary Fig. 14) indicate a binding adsorption effect between the surfactant molecules and the (002) plane of zinc.

- Concentration Increase: As zinc deposition continues, the surface concentration of adsorbed surfactant molecules increases, leading to significant accumulation and promoting structural transitions to minimize free energy.

- Formation of Gradient Structure: The transition from a thin layer to a thicker gradient phase (~400 nm) occurs as the local concentration of surfactant changes, driving the reorganization of surfactant molecules into more efficient spatial structures.

Critical Packing Parameter (CPP) and Phase Transition:

The Critical Packing Parameter (CPP)[24] determines the type of interphase formed and is given by the formula:

$$CPP = V/(a_0 \cdot l)$$

where: V is the volume of the hydrophobic tail, a_0 is the effective headgroup area, l is the length of the hydrophobic tail.

- High Concentration Region (near zinc surface): In this region, the surfactant molecules are closely packed, reducing the headgroup area and increasing the CPP, favoring the formation of lamellar structures.
- Low Concentration Region (further from zinc surface): Here, the surfactant molecules are more loosely packed, increasing the headgroup area and decreasing the CPP, favoring the formation of hexagonal structures.

Thus, the in-situ formation of a gradient liquid crystal interphase is driven by the concentration gradient of the surfactant molecules and their dynamic reorganization to minimize free energy. The transition from hexagonal to lamellar structures is a result of varying local concentrations and the corresponding changes in the CPP. This intricate interplay between concentration and structure explains why we observe a gradient rather than a repeating lamellar structure.

Note that Zn should always deposit beneath the surfactant layer. This occurs because the surfactant layer (or liquid crystal) is an ionic conductor but lacks electronic conductivity similar to solid state interphase (SEI) layer in lithium batteries[25,26]. More specifically, the surfactant molecules we selected consist of hydrophilic polyoxyethylene groups and hydrophobic long-chain alkyl groups. This molecular structure lacks a continuous conductive conjugated π-electron system, thus it does not exhibit electrical conductivity and overall presents insulating properties[27]. The liquid crystal phase is formed by weak interactions such as van der Waals forces and hydrogen bonds, which do not generate free charge carriers, resulting in low conductivity. Although the liquid crystal layer has insulating properties and has the risk of dielectric breakdown, because the voltage we apply is not very high, dielectric breakdown will basically not occur[28,29]. However, the liquid crystal phase has an ordered molecular arrangement and specific pore structures that allow ions to migrate. These molecular arrangements create pathways for ions, enabling ion conduction under an electric field[30].

Supplementary Note 2.

Here's a detailed explanation about possible phase change mechanism:

First, let's introduce the structures of the two phases. ε-MnO_2 has a typical tunnel structure with 1x1 and 1x2 tunnels, while δ-MnO_2 has a layered structure similar to 2D materials[31]. The layered polymorphs are constructed by edge-sharing [MnO_6] octahedra across the basal plane, whereas tunnel polymorphs contain both edge-sharing and corner-sharing [MnO_6] units. Interestingly, both belong to hexagonal symmetry, but δ-MnO_2 shows a more ordered arrangement along the c-axis, with a more pronounced (002) plane and higher electronic conductivity (ε: 2 mS m^{-1}; δ: 3.7 mS m^{-1})[32], which is beneficial for deposition/stripping reactions.

Despite this, ε-MnO_2, typically formed in the pristine electrolyte, is considered the thermodynamically stable phase[32,33], while δ-MnO_2 is considered metastable under standard conditions. Thus, generating and maintaining the metastable phase is challenging.

From our experimental results, although we maintained identical electrochemical deposition conditions in the full cell, we observed ε-MnO_2 in the pristine electrolyte and δ-MnO_2 in the presence of the surfactant (Fig. 4a and 4b in our main text). We believe the surfactant alters the local chemical environment, affecting the nucleation and growth of MnO_2 crystals, leading to different MnO_2 polymorphs.

Combining our study on the zinc anode, we used various soft matter characterization techniques to detail the surfactant self-assembly process. We found that the initial single surfactant bilayer aids uniform MnO_2 nucleation (Supplementary Fig. 18), possibly facilitating the formation of the more ordered δ phase. The surfactant's hydrophilic end, similar to polyethylene glycol (PEG) chains, has been reported to enhance δ-MnO_2 yield in hydrothermal synthesis[34], suggesting its potential role in reducing nucleation barriers.

More importantly, for the subsequent growth phase, DFT calculations simulated the adsorption of surfactant molecules on different MnO_2 crystal planes, considering electrolyte pH and full cell voltage conditions (Supplementary Figs. 20 and 21). DFT results showed that, compared to the (100) plane, surfactant molecules preferentially adsorb on the δ-MnO_2 (002) plane, forming C-O bonds (Supplementary Fig. 21). This adsorption leads to surfactant accumulation and the formation of a liquid crystal interphase (Fig. 4c), which acts as a soft template. This process modifies growth thermodynamics and kinetics, favoring the more ordered δ-MnO_2 over ε-MnO_2.

This process may resemble van der Waals epitaxy[35,36], where the liquid crystal phase creates a van der Waals interface, aligning with the (002) planes to promote δ-MnO_2 growth and reduce the energy barrier for this specific orientation. Van der Waals epitaxy doesn't require high lattice matching; low interfacial energy between the liquid crystal interphase and δ-MnO_2 reduces interface stress and defects considering that both have a layered structure and interact mainly through van der Waals forces, aiding epitaxial growth.

Back to the metastability issue again, the δ-MnO_2 phase formed with the surfactant is metastable. A metastable phase is not the lowest energy state but remains stable due to kinetic barriers preventing transformation to the stable phase. The liquid crystal phase may hinder the layer-to-tunnel (L-T) transition[37], maintaining the metastable δ-MnO_2. Additionally, proton consumption on the cathode side leads to the ZHS formation, and in the surfactant electrolyte, reduced ZHS (Supplementary Figs. 22 and 23) help maintain the weakly interacting δ phase[38], while the porous ZHS as nucleation layer formed in the pristine electrolyte might induce porous ε-MnO_2[39].

Supplementary Note 3.

The properties of surfactants essential for building an effective liquid crystal interface are multifaceted. These properties are crucial not only for forming stable and functional liquid crystals but also for ensuring compatibility with battery application. Here are the possible key criteria:

- Proper Hydrophilic and Hydrophobic Groups: A surfactant must possess a well-balanced amphiphilic structure to drive self-assembly into liquid crystals. The hydrophilic (water-attracting) and hydrophobic (water-repelling) components of the surfactant must be optimized to form interphases at particular concentrations and temperatures. This balance influences the morphology of the liquid crystal phases that can be formed, such as lamellar, cubic, or hexagonal structures. Besides, the primary factors influencing lyotropic phase structures include electrostatic interactions, hydration of surfactant head groups, steric repulsions, and the conformations of alkyl chains[40].
- Reducing Interference with Ion Transport: Particularly in applications like zinc-based batteries, it is critical that the surfactant's molecular groups do not significantly hinder the mobility of ions, such as zinc ions, within the electrolyte. The structural arrangement of the surfactant should facilitate, rather than obstruct, the desired ionic movements and interactions at the electrode interfaces. The construction of orderly water channels is often also important[41] because it may provide potential ion diffusion pathways.
- Chemical and Electrochemical Stability: In complex solution environments, the surfactant should possess high stability under operational conditions to prevent its decomposition or reaction within the system. For battery applications, this stability is essential to withstand the electrochemical environment during battery charging and discharging cycles. The surfactant should be able to assemble into a liquid crystal structure without being degraded by the electrochemical processes involved.
- Compatibility with the Electrode Material: The surfactant should adsorb effectively onto the electrode surfaces without forming detrimental interactions. This adsorption not only helps in forming a stable interface but also plays a pivotal role in directing the growth and orientation of electrodeposited materials, such as zinc in battery anodes.
- Temperature and Concentration Flexibility: The effective range of temperatures and concentrations at which the surfactant can form liquid crystal structures is crucial. This flexibility ensures that the surfactant can maintain its functionality under varying operational conditions, which is particularly important for practical applications that might experience fluctuations in environmental conditions. The optimal surfactant concentration is likely around the critical micelle concentration (CMC) of the surfactant.

These properties together determine the effectiveness of surfactants in constructing liquid crystal interphases that are not only structurally and chemically stable but also functionally advantageous for specific applications, such as guiding the deposition in battery technologies. Each property plays a synergistic role in ensuring that the liquid crystal interface performs optimally within the intended application.

Supplementary References:

1. Cao, L.*, et al.* Fluorinated interphase enables reversible aqueous zinc battery chemistries. *Nature Nanotechnology* **16**, 902-910 (2021).
2. Fang, X.*, et al.* Patterning Liquid Crystalline Organic Semiconductors via Inkjet Printing for High-Performance Transistor Arrays and Circuits. *Advanced Functional Materials* **31**, 2100237 (2021).
3. Ye, X.*, et al.* Unraveling the deposition/dissolution chemistry of MnO 2 for high-energy aqueous batteries. *Energy & Environmental Science* **16**, 1016-1023 (2023).
4. Zheng, J.*, et al.* Reversible epitaxial electrodeposition of metals in battery anodes. *Science* **366**, 645-648 (2019).
5. Weiss, V., Thiruvengadathan, R. & Regev, O. Preparation and characterization of a carbon nanotube− lyotropic liquid crystal composite. *Langmuir* **22**, 854-856 (2006).
6. Oyafuso, M.H.*, et al.* Development and in vitro evaluation of lyotropic liquid crystals for the controlled release of dexamethasone. *Polymers* **9**, 330 (2017).
7. Ma, L.*, et al.* Toward Practical High-Areal-Capacity Aqueous Zinc-Metal Batteries: Quantifying Hydrogen Evolution and a Solid-Ion Conductor for Stable Zinc Anodes. *Advanced Materials* **33**, 2007406 (2021).
8. Yan, H., Li, S., Nan, Y., Yang, S. & Li, B. Ultrafast Zinc–Ion–Conductor Interface toward High-Rate and Stable Zinc Metal Batteries. *Advanced Energy Materials* **11**, 2100186 (2021).
9. Zeng, X.*, et al.* Electrolyte Design for In Situ Construction of Highly Zn2+-Conductive Solid Electrolyte Interphase to Enable High-Performance Aqueous Zn-Ion Batteries under Practical Conditions. *Advanced Materials* **33**, 2007416 (2021).
10. Efaw, C.M.*, et al.* Localized high-concentration electrolytes get more localized through micelle-like structures. *Nature Materials* **22**, 1531-1539 (2023).
11. Li, W., Tchelepi, H.A., Ju, Y. & Tartakovsky, D.M. Stability-guided strategies to mitigate dendritic growth in lithium-metal batteries. *Journal of The Electrochemical Society* **169**, 060536 (2022).
12. Li, W., Tchelepi, H.A. & Tartakovsky, D.M. Screening of Electrolyte-Anode Buffers to Suppress Lithium Dendrite Growth in All-Solid-State Batteries. *Journal of The Electrochemical Society* **170**, 050510 (2023).
13. Chen, C.-h., Postlethwaite, T.A., Hutchison, J.E., Samulski, E.T. & Murray, R.W. Electrochemical measurements of anisotropic diffusion in thin lyotropic liquid crystal films using interdigitated array electrodes. *The Journal of Physical Chemistry* **99**, 8804-8811 (1995).
14. Boso, F., Li, W., Um, K. & Tartakovsky, D.M. Impact of carbon binder domain on the performance of lithium-metal batteries. *Journal of The Electrochemical Society* **169**, 100550 (2022).
15. Li, W. & Tartakovsky, D.M. Effective representation of active material and carbon binder in porous electrodes. *Journal of The Electrochemical Society* **169**, 040556 (2022).
16. Rodríguez-Abreu, C. On the Relationships between the Hydrophilic–Lipophilic Balance and the Nanoarchitecture of Nonionic Surfactant Systems. *Journal of Surfactants and Detergents* **22**, 1001-1010 (2019).

17. Kovalchuk, N.M. & Simmons, M.J.H. Surfactant-mediated wetting and spreading: Recent advances and applications. *Current Opinion in Colloid & Interface Science* **51**, 101375 (2021).
18. Milne, A.J.B. & Amirfazli, A. Autophilic Effect: Wetting of Hydrophobic Surfaces by Surfactant Solutions. *Langmuir* **26**, 4668-4674 (2010).
19. Lee, K.S., Ivanova, N., Starov, V.M., Hilal, N. & Dutschk, V. Kinetics of wetting and spreading by aqueous surfactant solutions. *Advances in Colloid and Interface Science* **144**, 54-65 (2008).
20. Wang, F.*, et al.* Production of gas-releasing electrolyte-replenishing Ah-scale zinc metal pouch cells with aqueous gel electrolyte. *Nature Communications* **14**, 4211 (2023).
21. Xu, X.*, et al.* Overcoming Challenges: Extending Cycle Life of Aqueous Zinc‐Ion Batteries at High Zinc Utilization through a Synergistic Strategy. *Small*, 2308273 (2023).
22. Weiss, V., Thiruvengadathan, R. & Regev, O. Preparation and Characterization of a Carbon Nanotube−Lyotropic Liquid Crystal Composite. *Langmuir* **22**, 854-856 (2006).
23. Ahir, S.V., Petrov, P.G. & Terentjev, E.M. Rheology at the Phase Transition Boundary: 2. Hexagonal Phase of Triton X100 Surfactant Solution. *Langmuir* **18**, 9140-9148 (2002).
24. van 't Hag, L., Gras, S.L., Conn, C.E. & Drummond, C.J. Lyotropic liquid crystal engineering moving beyond binary compositional space – ordered nanostructured amphiphile self-assembly materials by design. *Chemical Society Reviews* **46**, 2705-2731 (2017).
25. Xu, K. Electrolytes and Interphases in Li-Ion Batteries and Beyond. *Chemical Reviews* **114**, 11503-11618 (2014).
26. Shi, F.*, et al.* Lithium metal stripping beneath the solid electrolyte interphase. *Proceedings of the National Academy of Sciences* **115**, 8529-8534 (2018).
27. Garbovskiy, Y. & Glushchenko, I. Nano-Objects and Ions in Liquid Crystals: Ion Trapping Effect and Related Phenomena. *Crystals* **5**, 501-533 (2015).
28. Dierking, I. Dielectric breakdown in liquid crystals. *Journal of Physics D: Applied Physics* **34**, 806 (2001).
29. Mozoļevskis, G. Dielectric Breakdown Of High Voltage Liquid Crystal Displays. (2017).
30. Kato, T.*, et al.* Transport of ions and electrons in nanostructured liquid crystals. *Nature Reviews Materials* **2**, 17001 (2017).
31. Liu, B., Sun, Y., Liu, L., Xu, S. & Yan, X. Advances in Manganese-Based Oxides Cathodic Electrocatalysts for Li–Air Batteries. *Advanced Functional Materials* **28**, 1704973 (2018).
32. Xiao, X.*, et al.* Ultrahigh-Loading Manganese-Based Electrodes for Aqueous Batteries via Polymorph Tuning. *Advanced Materials* **35**, 2211555 (2023).
33. Zhong, C.*, et al.* Decoupling electrolytes towards stable and high-energy rechargeable aqueous zinc–manganese dioxide batteries. *Nature Energy* **5**, 440-449 (2020).
34. Hong, S.*, et al.* Efficient Scalable Hydrothermal Synthesis of MnO2 with Controlled Polymorphs and Morphologies for Enhanced Battery Cathodes. *ACS Energy Letters* **8**, 1744-1751 (2023).
35. Lin, Z.*, et al.* Scalable solution-phase epitaxial growth of symmetry-mismatched heterostructures on two-dimensional crystal soft template. *Science Advances* **2**, e1600993 (2016).

36. Kum, H.*, et al.* Epitaxial growth and layer-transfer techniques for heterogeneous integration of materials for electronic and photonic devices. *Nature Electronics* **2**, 439-450 (2019).
37. Yuan, Y.*, et al.* Deciphering the atomic patterns leading to MnO2 polymorphism. *Chem* **5**, 1793-1805 (2019).
38. Li, Y.-F., Zhu, S.-C. & Liu, Z.-P. Reaction Network of Layer-to-Tunnel Transition of MnO2. *Journal of the American Chemical Society* **138**, 5371-5379 (2016).
39. Mansley, Z.R.*, et al.* Mechanism of Chalcophanite Nucleation in Zinc Hydroxide Sulfate Cathodes in Aqueous Zinc Batteries. *Nano Letters* **23**, 8657-8663 (2023).
40. Tiddy, G.J.T. Surfactant-water liquid crystal phases. *Physics reports* **57**, 1-46 (1980).
41. Ishii, Y., Matubayasi, N., Watanabe, G., Kato, T. & Washizu, H. Molecular insights on confined water in the nanochannels of self-assembled ionic liquid crystal. *Science Advances* **7**, eabf0669 (2021).